Silicon (2022) 14:6097–6106
https://doi.org/10.1007/s12633-021-01278-y

ORIGINAL PAPER

Tunable Terahertz Wavelength Conversion Based on Optofluidic Infiltrated Rib Silicon Waveguides

H. Pakarzadeh [1] · S. Hosseinabadi [1] · I. S. Amiri [2]

Received: 29 March 2021 / Accepted: 14 July 2021 / Published online: 20 September 2021

Abstract

Terahertz (THz) sources have attracted special attention for various applications. Compared to the standard silica-based optical fibers, silicon waveguides have more advantages such as higher refractive index and lower absorption loss over the THz region. In this paper, for the first time, a rib silicon waveguide based on the photonic crystal (PC) idea is designed and by using the scalar modulation instability (SMI) phenomenon, tunable wavelength conversion for THz wave generation is simulated. By changing the structural parameters such as the air-hole diameter of the PC and infiltration of optical fluids into the air holes, linear and nonlinear characteristics of the waveguide are controlled and hence the generated THz radiation is considered as a tunable source. Simulation presents that the maximum converted wavelength, 326.17 μm, is obtained when the air-hole diameter is set at d = 0.86 μm and the pump wavelength is in the normal dispersion regime. Also, we have infiltrated optical fluids into PC air holes in order to change the dispersion properties of the waveguide while keeping the geometrical parameters unchanged. This led to converted wavelengths of 70.5, 76.8 and 107.5 μm, all located in the THz region. The loss of this waveguide is less than $0.8^{dB}/_{cm}$, which is less than that of previously reported in similar silicon waveguides.

Keywords Silicon waveguide · Photonic crystal · Optical fluids · Four-wave mixing · Dispersion engineering · Terahertz (THz)

1 Introduction

THz radiation as an electromagnetic radiation in the frequency range of 0.1 to 10 THz (wavelength range of 30 μm to 3 mm) has attracted a lot of interest in both science and technology [1]. The THz band which is located between the infrared and microwave region is a low energy and non-ionizing radiation that may penetrate in non-polar and non-metallic materials such as cloth, paper, stone and plastics [2].

The development of efficient THz wave sources is important for measurement applications and biology [3]. There are many methods for generating THz radiation such as: photoconductive antennas [4], large particle accelerators [5, 6], quantum cascade lasers [7], and optical rectification in nonlinear crystals [8, 9]. The important ones that have been recently used is four-wave mixing (FWM) in silicon waveguides [10].

Compared to the conventional silica-based optical fibers, a rib silicon waveguide is a more consistent structure for generating THz waves through the FWM. In fact silicon has more inherent advantages than silica so that the absorption loss of the silicon is less than 0.23 cm^{-1} in range of 1.2–6.9 μm and 25–200 μm [11], while absorption coefficient of optical fiber is 5 cm^{-1} in the THz region. Moreover, silicon nonlinear refractive index is 200 times greater than the silica [12] and also the silicon refractive index (about 3.5) is much larger than the air refractive index (about 1), which leads to a very strong light confinement. Additionally, the crystalline nature of silicon is in such a way that if the transverse magnetic (TM) mode is launched, the stimulated Raman scattering (SRS) does not occur, because this scattering strongly depends on the waveguide geometry and the mode polarization, so SRS cannot occur when an input pulse excites the TM mode [10]. Finally, the rib silicon waveguide is compatible with the CMOS technology which enables large-scale integration with a low cost [10]. Low cost, abundant availability as well as

✉ I. S. Amiri
irajsadeghamiri@tdtu.edu.vn

H. Pakarzadeh
pakarzadeh@sutech.ac.ir

S. Hosseinabadi
sh_hosseinabadi@yahoo.com

[1] Physics Department, Shiraz University of Technology, Shiraz, Iran

[2] Ton Duc Thang University, Ho Chi Minh City, Vietnam

good linear and nonlinear optical properties have made silicon as an ideal material for fabricating nanoscale photonic complex devices [13].

Owing to the interplay of nonlinear effects and dispersion, many nonlinear systems can exhibit an unstable phenomenon known as the modulation instability (MI) which leads to generation of new side bands [14]. MI is a third-order nonlinear phenomenon that can be utilized for wavelength conversion in optical fibers/waveguides [14]. The simplest form of MI is considered as scalar modulation instability (SMI) which has no dependency on the polarization state of the lightwave [14]. The underlying physics of SMI is the production of new photons which is known as Stokes and anti-Stokes. In the case of SMI, in order to satisfy the phase-matching condition, the pump wavelength (λ_p) must be adjusted very close to the zero-dispersion wavelength (ZDW), λ_0, of the waveguide in either normal ($\lambda_p < \lambda_0$) or anomalous ($\lambda_p > \lambda_0$) dispersion regimes [15].

In this paper, for the first time, we design a photonic crystal-based rib silicon waveguide to achive tunable wavelength conversion in the THz region. We examine wavelength conversion via the SMI phenomenon in both the anomalous and the normal dispersion regimes. To this end, we change the structural parameters (both geometry and optofluidic infiltration) of the waveguide to engineer the dispersion and nonlinear characteristics and hence to control the phase-matching condition and finally tune the converted wavelengths in THz region. As the wavelength conversion strongly depends on group-velocity dispersion (GVD) parameter, β_2, the merit of the optofluidic infiltration is to obtain tunable wavelength conversion while keeping the waveguide geometry unchanged.

The optical properties of fluids are generally very wide. An optical fluid can be applied to any photonic device which has an air hole in its structure [16, 17]. The fluid interacts with the confined field and changes the dispersion properties of device [17]. Fluid can be successfully infiltrated in photonic crystal (PC) and microstructures and change the waveguide properties. Most recently, the optofluidic infiltration in photonic crystal fibers (PCFs) has been used for wavelength conversion in the telecommunication region [15]. Therefore, in this work, we intend to investigate the wavelength conversion in the PC-based rib silicon waveguide to access the THz region not only with the help of geometrical changes but also with optofluidic infiltration possessing various refractive indices. In fact, by infiltrating the optofluidic into the PC air holes of the waveguide and changing the optical fluid's refractive index, n_F, the dispersion properties can be changed and thereby the converted wavelengths are tuned [18].

The paper structure is as below. In Section 2, the theoretical framework of the wavelength conversion in both anomalous and tnormal dispersion regimes based on the SMI is presented. In Section 3, we design a PC-based rib silicon waveguide and determine its linear and nonlinear characteristics. In Section 4, the wavelength conversion is simulated when geometrical parameters are changed or when the waveguide is infiltrated with various optical fluids. Finally, the paper is concluded in Section 5.

2 Theory of the Study

Modulation instablity (MI) is a general feature of the lightwave propagating in an optical medium where dispersion and nonlinear effects are simultaneously present. Based on MI, when a pump wave with the angular frequency of ω_p is input into the optical waveguide, the generated sidebands (Stokes and anti Stokes) are symmetrically located with resect to the pump frequency (zero detuning); so that the energy conservation condition will be met, i.e. $2\omega_p = \omega_a + \omega_s$. The angular frequencies of the sidebands, Stokes and anti Stokes, are defined respectively by ω_s and ω_a [15].

The frequency detuning of the sidebands with respect to the pump frequency is given by $\Omega = \omega_p - \omega_s = \omega_a - \omega_p$ where $\omega_s = \frac{2\pi c}{\lambda_s}$ *and* $\omega_a = \frac{2\pi c}{\lambda_a}$, and the Stokes and anti -Stokes wavelengths are presented by λ_s and λ_a, respectively [14, 15].

Linear stability analysis, phase-matching condition and FWM can be used to describe the SMI in an optical medium [14]. From the phase-matching condition, one can readily determine the peak frequency detunings Ω_{max} at which the maximum gain of SMI occurs, thus $\Delta k = \beta_2\Omega^2 + 2\gamma p_0 = 0$. Therefore, the position of peak frequency detunings in the anomalous dispersion regime are easily determined as [14, 15]:

$$\Omega_{\max} = \pm\sqrt{\frac{2\gamma p_0}{|\beta_2|}} \tag{1}$$

where p_0 is the peak power of the input pump and β_2 is the second-order dispersion coefficient of the waveguide which is calculated at pump wavelength, λ_p. Also, γ denotes the nonlinear parameter of the waveguide. In the normal dispersion regime, the mode propagation constant, β, should be expanded up to fourth order β_4 to determine Ω_{max} as [14, 15]:

$$\Omega_{max} = \pm\frac{\sqrt{-2\beta_4\left(3\beta_2 + \sqrt{9\beta_2^2 - 6\beta_4\gamma P_0}\right)}}{\beta_4} \tag{2}$$

where the phase-matching criterion, $\Delta k = \beta_2\Omega^2 + \frac{1}{12}\beta_4\Omega^4 + 2\gamma p_0 = 0$, is used. It should be noted that in the anomalous dispersion regime where β_2 is negative, the first term of $\Delta k = \beta_2\Omega^2 + 2\gamma p_0$ can be cancelled out by the second term (which is always positive), so the phase-matching condition is satisfied. On the other hand, in the normal dispersion regime, since β_2 is positive, the negative term corresponds to β_4 so that the phase-matching condition $\Delta k = \beta_2\Omega^2 + \frac{1}{12}\beta_4\Omega^4 + 2\gamma p_0 = 0$ is fulfilled.

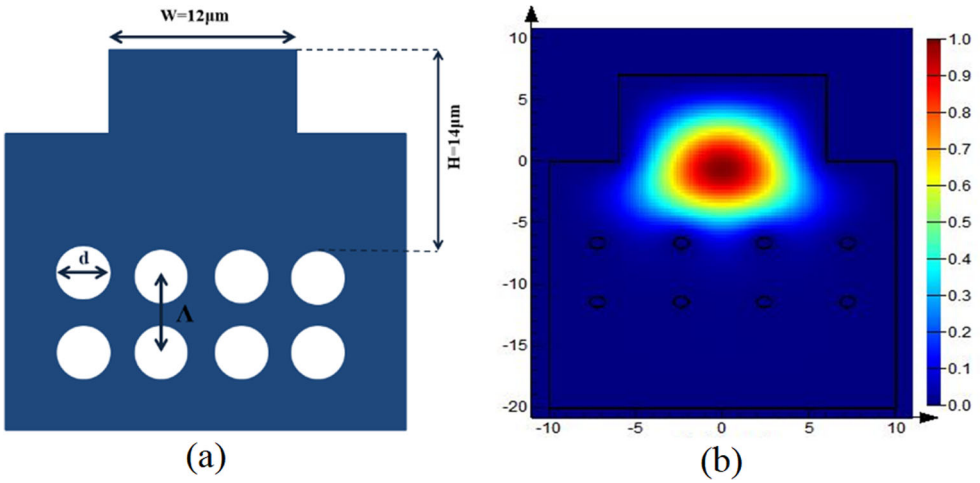

Fig. 1 (a) Cross-sectional view of the PC-based rib silicon waveguide; (b) distribution of the fundamental TM mode confined in the waveguide core. The air-hole diameter, d, can be changed for geometrical change of waveguide

The intensity gain coefficient of the SMI in the anomalous dispersion regime can be calculated as [14, 15]:

$$g(\Omega) = 2Im\left[\sqrt{\frac{1}{2}\beta_2\Omega^2\left(\frac{\beta_2\Omega^2}{2} + 2\gamma p_0\right)}\right] \quad (3)$$

Both theoretical and experimental investigations show that the SMI may occurs in the normal dispersion regime as well where the higher-order dispersion coefficients are taken into account. Therefore, considering dispersion terms up to the fourth-order coefficient β_4, the intensity gain coefficient in the normal dispersion regime becomes [14, 15]:

$$g(\Omega) = \frac{1}{12}Im\left[\left(\sqrt{\beta_4\Omega^4 + 12\beta_2} \times \sqrt{\beta_4\Omega^4 + 12\beta_2\Omega^2 + 48\gamma p_0}\right)\Omega\right] \quad (4)$$

It will be shown in Sectoin 4.2 that the converted wavelengths (generated sidebands) in the normal dispersion regime can be located in the THz region.

3 The PC-Based Rib Silicon Waveguide Design

In this section, we design for the first time a PC-based rib silicon waveguide with suitable dispersion characteristics and investigate the wavelength conversion in this waveguide for a given input pump wave. If the circular air-hole diameter of PC changes and hence the waveguide dispersion characteristics vary, the converted wavelength range will be tuned. The waveguide which is studied in this work is made of silicon in which wavelength-dependent refractive index is given as [19]:

$$n^2 - 1 = \frac{10.6684293\lambda^2}{\lambda^2 - (0.301516485)^2} + \frac{0.0030434748\lambda^2}{\lambda^2 - (1.13475115)^2} + \frac{1.54133408\lambda^2}{\lambda^2 - (1104)^2} \quad (5)$$

The guidance mechanism of the waveguide is the same as the standard optical fibers, which is the total internal reflection [20].

Our proposal of the PC-based rib silicon waveguide is shown in Fig. 1 (a). The PC is arranged as a rectangular array of circular air holes inside the silicon waveguide background and is located at a distance of 14 μm from the top of the waveguide. The lattice pitch of the PC is fixed at $\Lambda = 4.80$ μm and the wavelength conversion process is controlled by changing the diameter of the air holes. In Fig. 1 (b), the mode which is well confined within the waveguide core, is located above the PC air holes. The air-hole diameter, d, can be changed which leads to change of waveguide dispersion. It should be noted that a similar waveguide has been recently reported by Pakarzadeh et al. for the pulse propagation in the THz region [21].

We have simulated the fundamental mode field distribution and mode propagation constant of the proposed waveguide [22, 23]. A full-vectorial modal analysis based on the finite-difference eigenmode is used to obtain the field distribution of the fundamental mode and propagation constant of the waveguide [24, 25]. The method discretizes the waveguide cross section using a 100 numbers of mesh cells and mesh step of 1×10^{-6} μm in each direction and formulates Maxwell's equations in terms of a matrix eigenvalue problem. Perfectly matched layers with 18 μm width are used as absorbing boundaries placed on the boundary of the waveguide. Conformal meshing was also applied to all material interfaces to reduce meshing errors and increase the numerical accuracy of the simulations.

Table 1 The zero-dispersion wavelength (ZDW) of the PC-based rib silicon waveguide for various air-hole diameters

d(μm)	4.60	2.88	2.00	1.60	1.20	1.06	0.94	0.86
ZDW(μm)	5.65	5.80	5.90	6.00	6.10	6.20	6.30	6.40

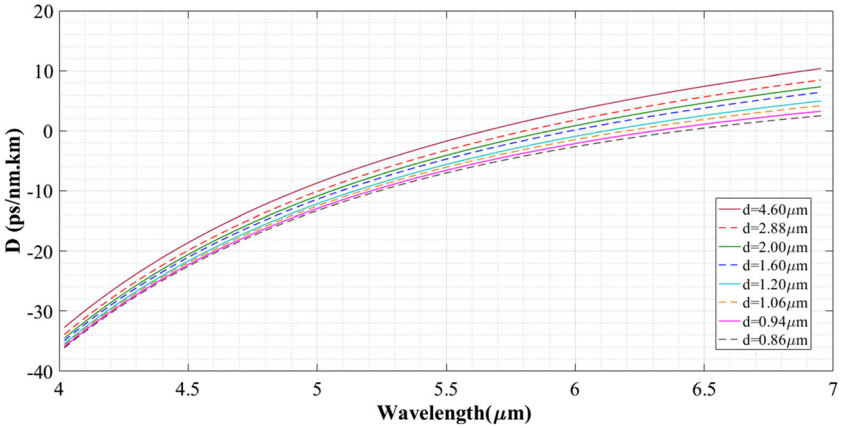

Fig. 2 Dispersion curves, D, versus wavelength for different air-hole diameters, d

It should be noted that our proposal is inspired by a silicon membrane waveguide reported by Z. Wang et al. to generate THz radiation which makes it possible to create new wavelengths only by changing the waveguie geometry [10]. However, our proposed PC-based rib silicon waveguide has more advantages than the silicon membrane waveguide or other designs [11], with unique features such as freedom in design owing to the PC air holes and much lower loss (less than $0.8^{dB}/_{cm}$,) in operating wavelengths. In addition, our waveguide enables generating new wavelengths not only by changing the geometry, but also by infilterating optofluidic into the PC air holes. This makes our waveguide more suitable for industrial and commercial purposes in comparison to previous ones.

Figure 2 shows dispersion curves, D, as a function of wavelength in the range of 4.0 to 7.0 μm for various air-hole diameters, d. As it is evident, by decreasing the diameter of the air holes, the zero-dispersion wavelength (ZDW) shifts toward larger wavelengths; therefore, by engineering the dispersion curves, it is possible to tune the frequency shift and also the gain of the converted wavelengths (see Eqs. (1)–(4)). The dependency of the ZDW on the air-hole diameter is given in Table 1.

4 Tunable Wavelength Conversion in the PC-Based Rib Silicon Waveguide

We simulate the tunable wavelength conversion by changing the waveguide geometry as well as by optofluidic infiltration in both normal and anomalous dispersion regimes. Then, the best situation for obtaining the wavelength conversion in the THz region is determined.

4.1 Tunable Wavelength Conversion Via Geometrical Change in Anomalous Dispersion Regime

As already mentioned, in the anomalous dispersion regime, β_2 becomes negative. By using the dispersion curves, D, shown in Fig. 2 and Table 1, if the pump wavelength λ_p sets at 6.60 μm, the second-order dispersion coefficient $\beta_2 = -\frac{\lambda^2}{2\pi c}D$, becomes negative. By taking the second derivative of the β_2 relative to the angular frequency, the fourth-order coefficient, β_4, can be obtained which is reported in ref. [26].

The GVD parameter β_2, effective mode area A_{eff} (Or more precisely, the area of the intense spot seen in Fig. 1 (b)) and nonlinear parameter of the PC-based rib silicon waveguide, γ, are listed in Table 2 for various air-hole diameters calculated at

Table 2 Linear as well as nonlinear parameters of the PC-based rib silicon waveguide for different diameters of air holes calculated at the pump wavelength of $\lambda_P = 6.60$ μm in the anomalous dispersion region

d (μm)	D $(^{ps}/_{nm.km})$	β_2 $\left(^{ps^2}/_{m}\right)$	A_{eff} (μm^2)	$\gamma\left(^{1}/_{W.m}\right)$
4.60	8.15	-1.89×10^{-1}	69.74	6.82×10^{-2}
2.88	6.38	-1.48×10^{-1}	78.80	6.04×10^{-2}
2.00	5.32	-1.23×10^{-1}	84.99	5.60×10^{-2}
1.60	4.48	-1.04×10^{-1}	88.70	5.36×10^{-2}
1.20	3.18	-7.36×10^{-2}	93.93	5.06×10^{-2}
1.06	2.49	-5.77×10^{-2}	96.84	4.91×10^{-2}
0.94	1.67	-3.87×10^{-2}	100.16	4.75×10^{-2}
0.86	1.00	-2.32×10^{-2}	103.03	4.62×10^{-2}

Table 3 Sidebands frequencies along with wavelength shifts for different air-hole diameters calculated at the pump wavelength of λ_P = 6.60 μm in the anomalous dispersion regime

d (μm)	ω_s (THz)	ω_a (THz)	$\Delta\lambda=\lambda_s-\lambda_P$ (μm)
4.60	266.37	304.39	0.47
2.88	265.17	305.60	0.50
2.00	264.07	306.69	0.53
1.60	262.64	308.13	0.57
1.20	259.16	311.61	0.67
1.06	256.21	314.56	0.75
0.94	250.36	320.40	0.92
0.86	240.79	329.98	1.22

6.60 μm (because, according to Table 1, at this wavelength, for all air-hole diameters, the anomalous dispersion regime is fulfilled, i.e., $\lambda_p > ZDW$), and $\gamma = \frac{n_2\omega_p}{cA_{eff}} = \frac{n_2}{\lambda_p}\frac{2\pi}{A_{eff}}$, where the nonlinear refractive index of silicon is $n_2 = 5 \times 10^{-18}\ m^2/W$ [10].

By decreasing the air-hole diameters of the PC, the core-cladding index contrast decreases soA_{eff} γ decreaese as well. Core-cladding index contrast means the difference between the refractive index of the core and that of the cladding so when the air-hole diameter of the PC in the cladding decreases, the core-cladding index contrast reduces as well. This is because of the core purely consists of Si with the refractive index of ~3.5 while the cladding consists of Si and/or air. When the air-hole diameter decreases, the contribution of the air in the cladding decreases and hence the refractive index of the cladding approaches to Si refractive index. This leads to the decrease in core-cladding index contrast.

Based on Eq. (1), in the anomalous dispersion regime, when the value of β_2 is smaller, the greater value of Ω_{max} is

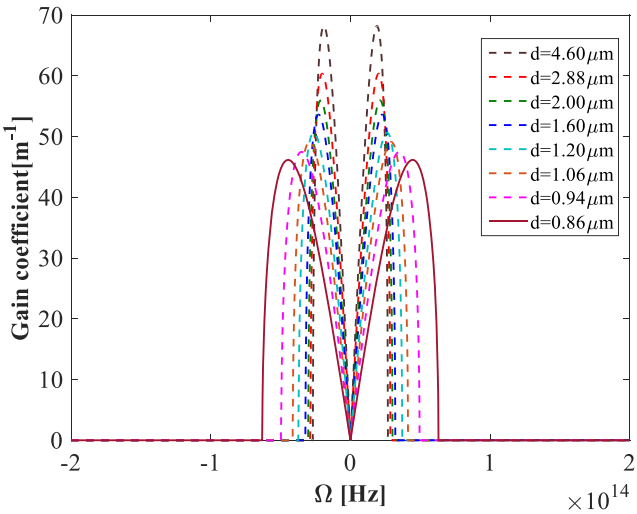

Fig. 3 Gain coefficient versus the frequency detuning for various air-hole diameters in the anomalous dispersion regime. The pump wavelength is set up at λ_P = 6.60 μm and the pump peak power is P_p = 500 W

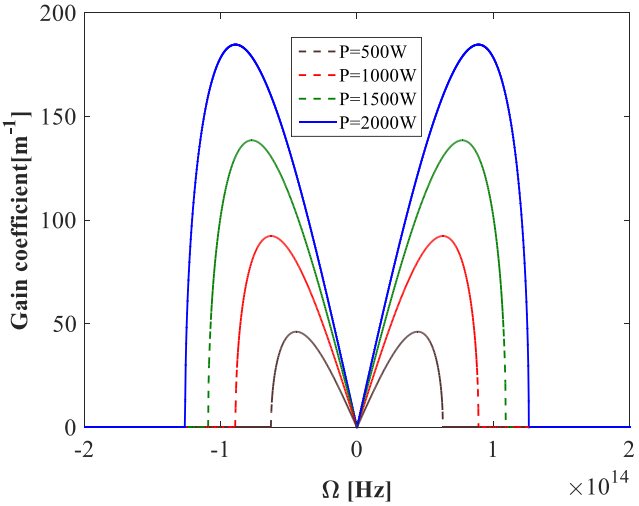

Fig. 4 The gain coefficient versus the frequency detuning for different pump peak powers in the anomalous dispersion regime. The air-hole diameter is fixed at d = 0.86 μm

obtained. Therefore, by decreasing the amount of β_2, the frequency shift of the sidebands increases. This can be seen in Table 2 where the smallest value of β_2 corresponds to the smallest diameter of the air hole. Table 3 lists the Stokes and anti-Stokes frequencies (ω_s and ω_a) as well as the wavelength shifts Δλ, where the pump wavelength is located at λ_P = 6.60 μm and the pump peak power is fixed at 500 W. According to Eq. (1), for smaller β_2, the larger Ω_{max} is occurred, hence the larger wavelength shift of 1.22 μm is obtained.

Figure 3 shows the gain coefficients as a function of the frequency detuning (Ω) simulated based on Eq. (3) for different air-hole diameters. According to Fig. 3, for d = 0.86 μm, the largest detuning corresponds to the smallest value of β_2 where the gain peak of the sidebands occurs. This has been already seen in Tables 2 and 3.

Based on Fig. 4, the gain coefficient increases. Additionally, increasing the pump power leads to shift the peak frequency detuning Ω_{max} to the larger values. This is because of increased nonlinear interaction and phase matching between the interacting waves. It is worth noting that the practical values of λ_p and P_p can be readily obtained via mid infrared sources operating between 3 and 8 μm; for example, the second-harmonic generation of the intense CO laser using the $ZnGeP_2$ crystal or coherent radiation based on difference-frequency generation from tunable optical parametric oscillators (OPOs) [27, 28].

As discussed above, in the PC-based rib silicon waveguide, it is possible to tune the converted wavelength by changing the waveguide geometry. In this case, the largest sideband peak was obtained for d = 0.86 μm at which β_2 has the smallest value, and correspondingly the largest wavelength shift of Δλ =1.22 μm is observed. Also, by increasing the pump peak

Table 4 Dispersion and nonlinear parameters of the PC-based rib silicon waveguide for different diameters of air holes at the pump wavelength of λ_P = 5.60 μm in normal dispersion regime

d (μm)	$\beta_2 \left(ps^2/m\right)$	$\beta_4 \left(ps^4/m\right)$	$A_{eff}((\mu m)^2)$	$\gamma \left(1/Wm\right)$
4.60	8.64×10^{-3}	-2.48×10^{-5}	68.94	8.13×10^{-2}
2.88	3.45×10^{-2}	-2.24×10^{-5}	77.84	7.20×10^{-2}
2.00	4.89×10^{-2}	-2.06×10^{-5}	83.86	6.69×10^{-2}
1.60	5.96×10^{-2}	-1.90×10^{-5}	87.37	6.42×10^{-2}
1.20	7.50×10^{-2}	-1.61×10^{-5}	92.06	6.09×10^{-2}
1.06	8.28×10^{-2}	-1.45×10^{-5}	94.60	5.93×10^{-2}
0.94	9.21×10^{-2}	-1.26×10^{-5}	97.32	5.76×10^{-2}
0.86	9.96×10^{-2}	-1.09×10^{-5}	99.58	5.63×10^{-2}

power for this fixed air-hole diameter, the frequency shift increases. Therefore, it is possible to control the location of the converted wavelengths by changing the air-hole diameter as well as the input pump peak power. However, as it is seen from the simulation results, the largest wavelength shift occurred in the anomalous dispersion regime cannot reach the THz region; therefore, one should examine the wavelength conversion in the normal dispersion regime.

4.2 Tunable Wavelength Conversion Via Geometrical Change in Normal Dispersion Regime

In this section, we change the pump wavelength from λ_P = 6.60 μm to λ_P = 5.60 μm and repeat simulations but for normal dispersion regime. As it can be seen from Table 1, when the pump wavelength is set at 5.60 μm, for all air-hole diameters the normal dispersion regime is fulfilled, i.e., $\lambda_p < ZDW$. In fact, in this regime, β_2 is positive and β_4 is negative [26]. The dispersion and nonlinear parameters of the PC-based rib silicon waveguide are listed in Table 4; while the wavelengths shift and Stokes and anti-stokes frequencies are given in Table 5.

Table 5 Stokes and anti-Stokes frequencies as well as the wavelength shifts for different air-hole diameters for the pump wavelength of λ_P = 5.60 μm in the normal dispersion regime

d (μm)	ω_s(THz)	ω_a (THz)	Δλ (μm)
4.60	243.12	429.60	2.15
2.88	193.57	479.15	4.13
2.00	163.87	508.85	5.90
1.60	139.55	533.17	7.90
1.20	98.47	574.25	13.54
1.06	73.37	599.35	20.09
0.94	38.99	633.73	42.74
0.86	5.78	666.94	320.57

As before, by decreasing the air-hole diameter, the core-cladding index contrast decreases soA_{eff} A_{eff} increases and simultaneously γ decreases. According to Eq. (2), in the normal dispersion regime, the peak frequency detuning depends on both the second- and the fourth-order dispersion coefficients so that for the largest β_2 and the smallest β_4, Ω_{max} will become maximum. As it is seen in Table 4, the largest β_2 and simultaneously the smallest β_4 are related to the smallest value of air-hole diameter of d = 0.86 μm. This leads to the maximum wavelength shift of Δλ = 320.57 μm which is given in Table 5.

As a result, it is desired to work in the normal dispersion regime to access new wavelengths in the THz region.

4.3 Tunable Wavelength Conversion Via Optofluidic Infiltration

As discussed above, one can control the waveguide dispersion curves by changing the geometrical parameters and hence tune the generated wavelength range. However, by infiltrating optical fluids with different refractive indices as the post-fabrication method, one can easily engineer linear and nonlinear characteristics of the waveguide to access the desired wavelength range. From the practical point of view, it is a more appropriate and optimal tool that enables us to achieve significant results via small manipulations. The variation of waveguide geometry is not an optimal method for reaching different wavelength regions, because one cannot practically use a waveguide with different air-hole diameters. Therefore, we should think about changing the dispersion properties of the waveguide in a different way, such as infiltrating optical fluids to access different wavelength regions while keeping the waveguide geometry unchanged.

In this section, we set the waveguide dimensions at fixed parameters of Λ = 4.8 μm and d = 0.86 μm, to ensure the largest wavelength shift as discussed in the previous section; and then infiltrate different optical fluids with various refractive indices in the PC air holes. To this end, we infiltrate water

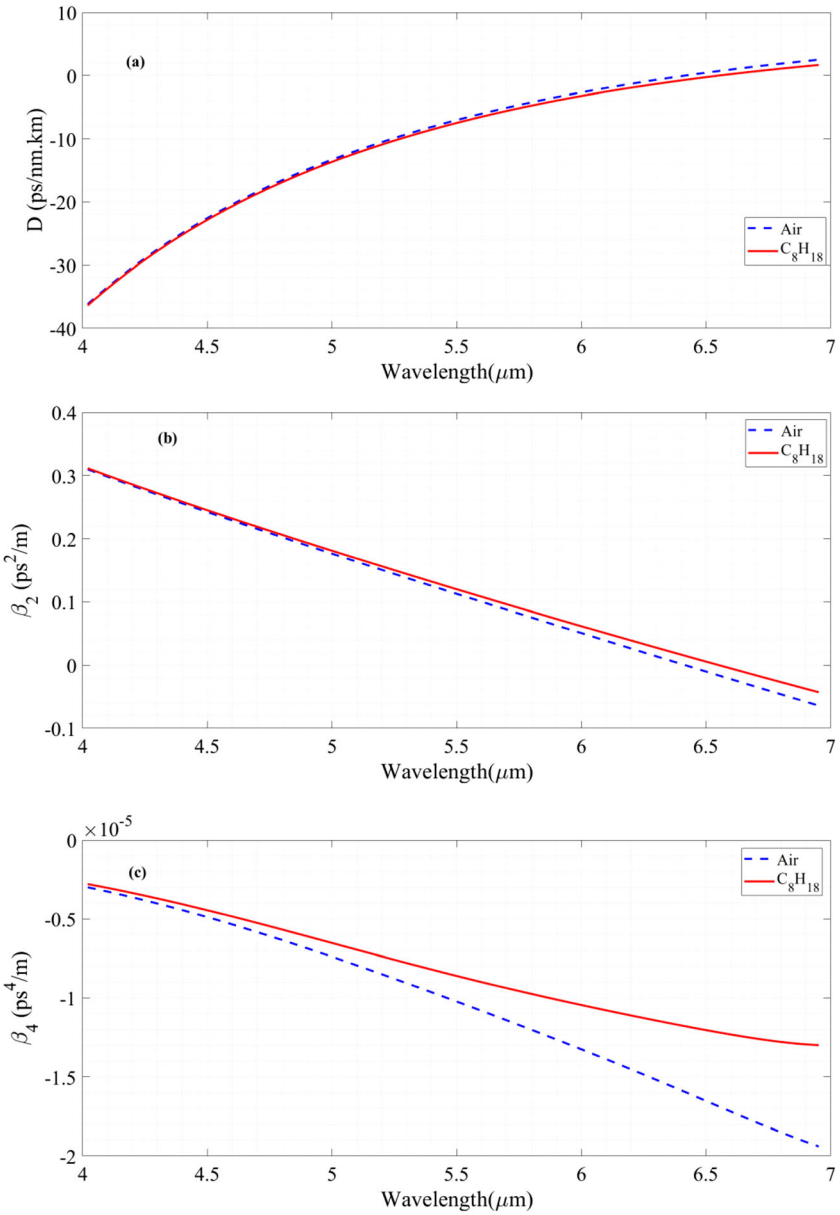

Fig. 5 Dispersion curves (a); GVD parameters (b); and fourth-order dispersion coefficients (c) for empty air hole (blue line) and optofluidic-infiltrated air hole (red line)

or other optical fluids into the PC air holes and then simulate β_2 and β_4 curves after that, compare them to the case of empty air holes (without infiltration). This is shown in Fig. 5 (a) whereby the refractive index of the holes increases, so the dispersion curve is changed and ZDW is shifted toward greater wavelengths. For instant, for the empty air hole, the ZDW is about 6.40 μm while for the optical fluid of C_8H_{18} this value is shifted to 6.56 μm.

As shown in Figs. 5 (b) and (c), β_2 and β_4 are plotted for both cases when the waveguide is uninfiltrated or infiltrated with various optical fluids. Evidently, by changing the refractive index of the fluid infiltrated into the PC air holes, the second- and fourth-order dispersion coefficients are changed and hence the wavelength shift is tuned according to Eq. (2).

Based on the obtained results in Sections 4–1 and 4–2, we obtain a larger wavelength shift for the normal dispersion

Table 6 Linear and nonlinear parameters of the PC-based rib silicon waveguide infiltrated by optical fluids with different refractive indices. The pump wavelength is set at $\lambda_P = 5.9$ μm in the normal dispersion regime

Optical fluid	$\beta_2 \left(ps^2/m\right)$	$\beta_4 \left(ps^4/m\right)$	$A_{eff}\,((\mu m)^2)$	$\gamma \left(1/W.m\right)$
Air	6.45×10^{-2}	-1.26×10^{-5}	100.77	5.29×10^{-2}
Water	7.27×10^{-2}	-1.05×10^{-5}	102.22	5.22×10^{-2}
C_5H_{12}	7.33×10^{-2}	-1.04×10^{-5}	102.32	5.21×10^{-2}
C_8H_{18}	7.45×10^{-2}	-1.01×10^{-5}	102.53	5.20×10^{-2}

Table 7 Stokes and anti-Stokes frequencies as well as the wavelength shifts of the PC-based rib silicon waveguide infiltrated by optical fluids with different refractive indices. The pump wavelength is set at $\lambda_P = 5.9$ μm in the normal dispersion regime

Optical fluid	ω_s (THz)	ω_a (THz)	$\Delta\lambda$ (μm)
Air	65.71	574.45	22.80
Water	26.75	613.42	64.59
C_5H_{12}	24.54	615.62	70.92
C_8H_{18}	17.54	622.62	101.58

regime. Therefore, in this section, simulations are only performed in the normal dispersion regime. Here, three different optical fluids including water, C_5H_{12} and C_8H_{18} are infiltrated into the PC air holes. The refractive indices of these fluids are as $n_{water} = 1.33400$ [29], $n_{C_5H_{12}} = 1.35377$ [30] and $n_{C_8H_{18}} = 1.39125$ [30]. The pump wavelength is set at $\lambda_P = 5.9$ μm, where for all cases the normal dispersion regime, $\lambda_P < ZDW$, takes place and therefore the second-order dispersion coefficient is positive and simultaneously the fourth-order dispersion coefficient is negative.

The linear and nonlinear parameters for all cases of unfiltrated and infiltrated PC holes are listed in Table 6 and corresponding wavelengths shifts, Stokes and anti-stokes frequencies are given in Table 7.

By increasing the refractive index of the air holes through the injection of optical fluid, the index contrast between the core and cladding decreases, soA_{eff} A_{eff} increases and γ decreases. As mentioned above, according to Eq. (2), in the normal dispersion regime, the peak frequency shift depends on both second- and fourth-order dispersion coefficients thus when β_2 is larger and β_4 is smaller, Ω_{max} will be larger than before as well. As seen in Table 6, the largest value of β_2 and the smallest value of β_4 correspond to the case of C_8H_{18} where according to Table 7, this leads to the largest wavelength shift of $\Delta\lambda = 101.58$ μm. This largest wavelength shift corresponds to the maximum converted wavelength of $\lambda = 107.48$ μm which lies in the THz region.

Figure 6 shows a gain coefficient versus the frequency detuning simulated based on Eq. (4) for both cases of C_8H_{18} optofluidic infiltration and empty air holes. As it is obvious, by infiltrating the optical fluids, the sideband peak frequency detuning is larger compared to that of the empty air hole. Therefore, the designed PC-based rib silicon waveguide can generate different wavelength shifts by changing the refractive index of the air holes via optofluidic infiltration. This provides

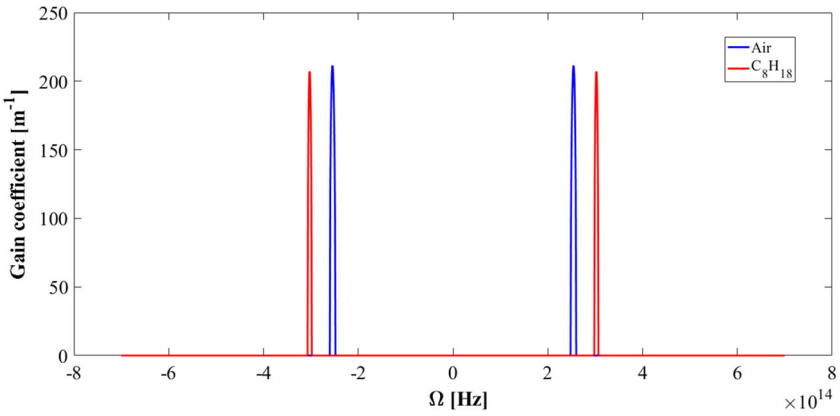

Fig. 6 Gain coefficient versus the frequency detuning for thr empty air hole (blue line) and the optofluidic infiltrated air hole (red line). The pump wavelength is set at $\lambda_P = 5.9$ μm in the normal dispersion regime with the pump peak power of $P_p = 2$ kW

an efficient method to access the THz region without changing the geometrical parameters.

5 Conclusion

In this paper, a rib silicon waveguide based on the photonic crystal (PC) idea was designed for the first time and tunable wavelength conversion for generating the THz radiation was simulated. As a result, the converted frequencies/wavelengths can easily lie in the THz region. When the pump wavelength is set at $\lambda_p = 5.60$ μm in the normal dispersion regime and for the fixed lattice pitch of $\Lambda = 4.80$ μm, as the air-hole diameter is changed from $d = 4.60$ μm to $d = 0.86$ μm, the converted wavelength is tuned from $\lambda = 2.15$ μm to $\lambda = 326.17$ μm, respectively. This is while for the pump wavelength of $\lambda_p = 5.9$ μm and the fixed lattice pitch of $\Lambda = 4.80$ μm and air-hole diameter of $d = 0.86$ μm, by infiltrating the optical fluids with different refractive indices in the PC air holes, the converted wavelength is tuned over the THz range from 70.5 μm to 107.5 μm.

Author's Contributions All authors contributed to the study conception and design. Material preparation, simulation results and analysis were performed by H. Pakarzadeh and S. Hosseinabadi. The first draft of the manuscript was written by S. Hosseinabadi and all authors commented on previous versions of the manuscript. All authors read and approved the final manuscript.

Data Availability Data are available on request from the authors.

Declarations Compliance with ethical standards is followed by authors.

Informed Consent Not applicable.

Consent to Participate Not applicable.

Consent for Publication Not applicable.

Conflict of Interest The authors declare that they have no potential conflicts of interests.

Research Involving Human Participants and/or Animals Not applicable.

References

1. Zhang XC, Xu J, (2010) Introduction to THz wave photonics. Springer; New York.
2. Pawar AY, Sonawane DD, Erande KB, Derle DV (2013) Terahertz technology and its applications. Drug Invent. Today. 5(2):157–163
3. Lewis RA (2014) A review of terahertz sources. J. Phys. D J Phys D Appl Phys. 47(37):374001 (11pp)
4. Burford NM, El-Shenawee MO, (2017) Review of terahertz photoconductive antenna technology. Opt. Eng. 56(1):010901(21pp).
5. Yang X, Brunetti E, Jaroszynski DA (2018) High-energy coherent terahertz radiation emitted by wide-angle electron beams from a laser-wakefield accelerator. New J. Phys. 20(4):043046
6. Evain C, Szwaj C, Roussel E, Rodriguez J, Le Parquier M, Tordeux MA, Ribeiro F, Labat M, Hubert N, Brubach JB, Roy P (2019) Stable coherent terahertz synchrotron radiation from controlled relativistic electron bunches. Nat. Phys. 15(7):635–639
7. Franckié M, Faist J (2020) Bayesian optimization of terahertz quantum cascade lasers. Phys. Rev. Appl. 13(3):034025
8. Ravi K, Huang WR, Carbajo S, Nanni EA, Schimpf DN, Ippen EP, Kärtner FX (2015) Theory of terahertz generation by optical rectification using tilted-pulse-fronts. Opt. Express 23(4):5253–5276
9. Piyathilaka HP, Sooriyagoda R, Dewasurendra V, Johnson MB, Zawilski KT, Schunemann PG, Bristow AD (2019) Terahertz generation by optical rectification in chalcopyrite crystals ZnGeP 2, CdGeP 2 and CdSiP 2. Opt. Express 27(12):16958–16965
10. Wang Z, Liu H, Huang N, Sun Q, Wen J (2012) Efficient terahertz-wave generation via four-wave mixing in silicon membrane waveguides. Opt. Express 20(8):8920–8928
11. Soref RA, Emelett SJ, Buchwald WR (2006) Silicon waveguided components for the long-wave infrared region. *J. Opt. A: Pure Appl. Opt.* 8(10):840–848
12. Yin L, Lin Q, Agrawal GP (2007) Soliton fission and supercontinuum generation in silicon waveguides. Opt. Lett. 32(4):391–393
13. Driscoll JB, Osgood RM, Grote RR, Dadap JI, Panoiu NC (2015) Squeezing light in wires: fundamental optical properties of Si nanowire waveguides. J. Light. Technol. 33(14):3116–3131
14. Agrawal GP (2013) Nonlinear Fiber Optics5th edn. *Academic Press*, *San Diago*
15. Pakarzadeh H, Derakhshan R, Hosseinabadi S, (2019) Tunable wavelength conversion based on optofluidic infiltrated photonic crystal fibers. J. Nonlinear Opt. Phys. Mater. 28(01): 1950002(17pp).
16. Psaltis D, Quake SR, Yang C (2006) Developing optofluidic technology through the fusion of microfluidics and optics. Nature 442(7101):381–386
17. Ebnali-Heidari M, Dehghan F, Saghaei H, Koohi-Kamali F, Moravvej-Farshi MK (2012) Dispersion engineering of photonic crystal fibers by means of fluidic infiltration. J. Mod. Opt. 59(16): 1384–1390
18. Bedoya AC, Domachuk P, Ting J, Grillet C, Monat C, Tomljenovic-Hanic S, Lee MW, McPhedran RC, Eggleton BJ, (2010) Optofluidic dispersion engineering of photonic crystal waveguides. In Conference on Lasers and Electro-Optics 2010 May 16 (p. CWM4). Optical Society of America.
19. Tatian B (1984) Fitting refractive-index data with the Sellmeier dispersion formula. Appl. Opt. 23(24):4477–4485
20. Crisp J and Elliott B, (2005) Introduction to fiber optics. 3rd Edition, Elsevier.
21. Pakarzadeh H, Akbari F (2021) Propagation of Terahertz Pulses in Photonic Crystal-Based Rib Silicon Waveguides. Silicon. https://doi.org/10.1007/s12633-021-01092-6
22. Zhu Z, Brown TG (2002) Full-vectorial finite-difference analysis of microstructured optical fibers. Opt. Express. 10(17):853–864
23. Pakarzadeh H, Rezaei SM, Namroodi L (2019) Hollow-core photonic crystal fibers for efficient terahertz transmission. Opt. Commun. 433:81–88
24. Saitoh K, Koshiba M (2005) Numerical modeling of photonic crystal fibers. J. Light. Technol. 23(11):3580–3590
25. Pakarzadeh H, Rezaei SM (2016) Modeling of dispersion and nonlinear characteristics of tapered photonic crystal fibers for applications in nonlinear optics. J. Mod. Opt. 63(2):151–158
26. Pakarzadeh H, Hosseinabadi S, Amiri IS, (2019) Designing a silicon waveguide for tunable wavelength conversion in terahertz region. In Seventh International Conference on Optical and Photonic

Engineering 2019 Oct 16 (Vol. 11205, p. 1120504). International Society for Optics and Photonics.
27. Ionin AA, Kinyaevskii IO, Klimachev YM, Kozlov AY, Kotkov AA (2017) A Broadband Infrared Laser Source (2.5–17 μm) for Plasma Diagnostics. Phys. At Nucl. 80(11):1635–1641
28. Sorokina IT, Ebrahim-Zadeh M, (2008) Mid-Infrared Coherent Sources and Applications. Springer Netherlands.
29. Hale GM, Querry MR (1973) Optical constants of water in the 200-nm to 200-μm wavelength region. Appl. Opt. 12(3):555–563
30. Anderson MR, (2000) Determination of infrared optical constants for single component hydrocarbon fuels. MISSOURI UNIV-ROLLA, (Master Thesis).